



## RESEARCH ARTICLE

# Detection of non-native species formed during fibrillization of the myocilin olfactomedin domain

Hailee F. Scelsi<sup>1</sup> | Emily G. S. Close<sup>1,2</sup> | Dustin J. E. Huard<sup>1</sup> | Elijah Dunn<sup>1</sup> |  
 Nebojša Bogdanović<sup>3</sup> | Sonali H. W. Mudiyansele<sup>4,5</sup> | Arshay Grant<sup>6</sup> |  
 Scott M. Stagg<sup>3,7</sup> | Ingeborg Schmidt-Krey<sup>6</sup> | Wade D. Van Horn<sup>4,5</sup>  |  
 Raquel L. Lieberman<sup>1</sup> 

<sup>1</sup>School of Chemistry and Biochemistry, Georgia Institute of Technology, Atlanta, Georgia, USA

<sup>2</sup>Pacific Northwest National Laboratory, Richland, Washington, USA

<sup>3</sup>Institute of Molecular Biophysics, Florida State University, Tallahassee, Florida, USA

<sup>4</sup>Biodesign Center for Personalized Diagnostics, Arizona State University, Tempe, Arizona, USA

<sup>5</sup>School of Molecular Sciences, Arizona State University, Tempe, Arizona, USA

<sup>6</sup>School of Biological Sciences, Georgia Institute of Technology, Atlanta, Georgia, USA

<sup>7</sup>Department of Biological Sciences, Florida State University, Tallahassee, Florida, USA

## Correspondence

Raquel L. Lieberman, School of Chemistry and Biochemistry, Georgia Institute of Technology, Atlanta, GA 30318, USA.  
 Email: [raquel.lieberman@chemistry.gatech.edu](mailto:raquel.lieberman@chemistry.gatech.edu)

## Funding information

U.S. Department of Energy, Grant/Award Number: DE-SC0012704; National Institute of General Medical Sciences, Grant/Award Numbers: R24GM145964, R35GM141933, S10\_OD027000, S10\_RR028976, S10\_RR25528, UL1TR000454; National Eye Institute, Grant/Award Number: R01EY021205

Review Editor: Jean Baum

## Abstract

Glaucoma is a group of neurodegenerative diseases that together are the leading cause of irreversible blindness worldwide. Myocilin-associated glaucoma is an inherited form of this disease, caused by intracellular aggregation of misfolded mutant myocilin. In vitro, the myocilin C-terminal olfactomedin domain (OLF), the relevant domain for glaucoma pathogenesis, can be driven to form amyloid-like fibrils under mild conditions. Here we characterize a species present during in vitro fibrillization. Purified OLF was subjected to fibrillization at concentrations required for downstream electron microscopy imaging and NMR spectroscopy. Additional biophysical techniques, including analytical ultracentrifugation and X-ray crystallography, were employed to further characterize the multicomponent mixture. Negative stain transmission electron microscopy (TEM) shows a non-native species reminiscent of known prefibrillar oligomers from other amyloid systems, NMR indicates a minor population of partially misfolded species is present in solution, and cryo-EM imaging shows two-dimensional protein arrays. The predominant soluble species remaining in solution after the fibril reaction is natively folded, as evidenced by X-ray crystallography. In summary, after incubating OLF under fibrillization-promoting conditions, there is a heterogeneous mixture consisting of soluble folded protein, mature amyloid-like fibrils, and partially misfolded intermediate species that at present belie additional molecular detail. The characterization of OLF fibrillar species illustrates the challenges associated with developing a comprehensive understanding of the fibrillization process for large, non-model amyloidogenic proteins.

## KEYWORDS

amyloid, biophysical characterization, glaucoma, misfolding, olfactomedin, oligomerization

## 1 | INTRODUCTION

For globular amyloidogenic proteins, the fibrillization pathway from native protein to end-point fibrils is thought to include intermediate species such as

oligomers and protofibrils (Fändrich 2012). The evolution from oligomer to protofibril to fibril results in a heterogeneous mixture of species that can be challenging to characterize in detail (Chiti and Dobson 2017). Studies of neurodegenerative diseases associated with

This is an open access article under the terms of the [Creative Commons Attribution-NonCommercial](https://creativecommons.org/licenses/by-nc/4.0/) License, which permits use, distribution and reproduction in any medium, provided the original work is properly cited and is not used for commercial purposes.

© 2025 The Author(s). *Protein Science* published by Wiley Periodicals LLC on behalf of The Protein Society.

amyloid formation suggest that soluble oligomeric assemblies are more toxic than their corresponding mature fibrils and could underlie the corresponding cytotoxicity and disease etiology (Kayed et al. 2003). Thus, understanding the fibrillization pathway and nature of intermediate species may open up new opportunities for therapeutic intervention.

Myocilin-associated glaucoma is a relatively recent addition to the list of diseases associated with protein misfolding and amyloid formation (Hill et al. 2014; Orwig et al. 2012). Mutations in myocilin, specifically within its 30 kDa C-terminal olfactomedin (OLF) domain, are associated with primary open-angle glaucoma (POAG). Autosomal-inherited mutations in myocilin are among the most common causal genetic links to glaucoma. Whereas glaucoma is normally a disease affecting individuals older than 40 years of age, myocilin-associated glaucoma affects ~3 million children and young adults worldwide (Wiggs and Pasquale 2017). In the anterior eye segment, the expression of mutant myocilin in trabecular meshwork (TM) cells leads to misfolding and subsequent cytotoxicity (Joe et al. 2003; Yam et al. 2007). TM cell death often occurs in POAG (Stamer and Clark 2017), but the presence of mutant myocilin leads to an accelerated timeline for disease progression.

WT OLF is a 5-bladed  $\beta$ -propeller (Donegan et al. 2015) that can be driven to fibrillize under mildly destabilizing conditions such as modestly increased temperature, gentle agitation, and mildly acidic pH (Hill et al. 2014). WT OLF fibrils exhibit numerous hallmarks of amyloid *in vitro* and have been characterized by various techniques including thioflavin T (ThT) fluorescence, atomic force microscopy (AFM), transmission electron microscopy (TEM) imaging, Fourier-transfer infrared (FTIR) spectroscopy, and A11 antibody staining (Hill et al. 2014; Orwig et al. 2012). A subset of residues that make up the fibril core has also recently been identified (Hill et al. 2014; Saccuzzo et al. 2024a). WT OLF follows an inside-out unfolding process with urea denaturation that is also observed for disease-associated OLF mutants (Saccuzzo et al. 2024b). For these reasons WT OLF is a suitable starting point for further studies of OLF fibrillization.

In this study, we sought to increase our understanding of OLF fibrillization, focusing on detecting intermediate species in the fibrillization pathway. We show that the heterogeneous mixture obtained upon forming fibrils of purified wild-type OLF contains ThT-positive insoluble endpoint fibrils, and a supernatant comprising leftover folded wild-type OLF and a minor component of partially folded species. Our study emphasizes the transient nature of on-pathway oligomers and demonstrates complexities associated with studying the heterogeneous process of fibrillization, particularly for large, non-model amyloid systems.

## 2 | RESULTS

### 2.1 | De novo fibril formation

To produce OLF fibril samples at concentrations needed for downstream analysis (Figure 1a), purified OLF (200  $\mu$ L of 200  $\mu$ M WT OLF in a 0.65 mL microcentrifuge tube) was incubated at 37°C with gentle rocking. This experimental procedure is ~10 $\times$  scaled down from our previous studies (Hill et al. 2014), but with the same relative head space in the microcentrifuge tube and similar growth kinetics. After incubation for ~66 h, the initially clear solution appeared cloudy, and the mixture reaches a ThT fluorescence plateau (Figure 1b). The fibrillization midpoint is ~25 h, mirroring our previous studies (Hill et al. 2014).

We analyzed the post-incubation sample by ThT fluorescence, TEM, and SDS-PAGE analysis of multiple fractions of the completed reaction mixture (Figure 1a). After a small amount of the initial end-point fibril mixture was set aside, the remainder of the sample was centrifuged, to obtain clarified supernatant and pellet for further analysis. The insoluble pellet after centrifugation was washed with buffer and then imaged by TEM, confirming the presence of a fibrillar species (Figure 1c). The clarified supernatant exhibits a fluorescence level ~35% of the end-point fibril mixture, and syringe filtration further decreases the ThT fluorescence (Figure 1d). Denaturing SDS-PAGE analysis of the sample post-incubation shows that the only species present in all four samples is monomeric OLF. Notably, there is a lack of any higher-order species at the stacking-resolving gel interface (Figure 1e). This is true even for the end-point fibril mixture, perhaps because this sample was substantially diluted for SDS-PAGE analysis. In summary, the scaled-down OLF fibrillization reaction exhibits typical sigmoidal growth but does not consume all of the available monomer for conversion to ThT-positive fibrils, leaving excess OLF in solution.

### 2.2 | EM imaging of OLF fibril sample reveals preparation-dependent higher-order species

Negative stain TEM imaging of the end-point fibril mixture after 66 h, prior to centrifugation, shows a few mature fibrils surrounded by numerous small (~10 nm) particles with an apparent central pore (Figure 2a). Since WT OLF (30 kDa monomer) is only ~4 nm in diameter and does not have an accessible central pore (Donegan et al. 2015), we hypothesized that this was a novel species, possibly a dimer or tetramer, meriting further characterization.

Subsequent cryo-EM analysis of the same sample, however, did not show a species consistent with that

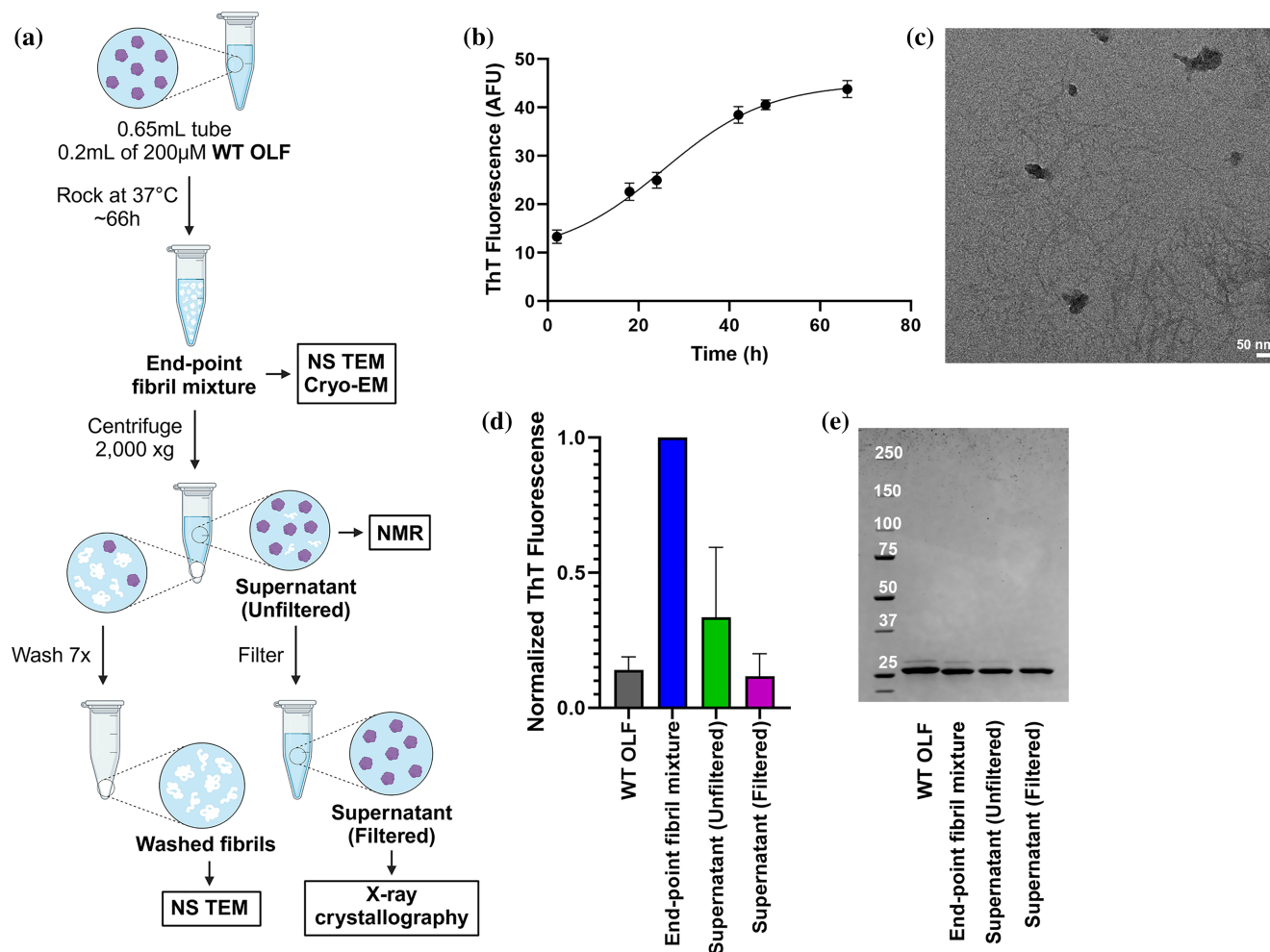


**FIGURE 1** Fibrillization yields ThT-positive insoluble OLF fibrils as well as soluble OLF. (a) Schematic representation of reaction fractions and analyses. (b) ThT fluorescence as a function of incubation time. Error bars denote standard error from analytical replicates. (c) Negative stain TEM image of washed insoluble end-point fibrils. Scale bar: 50 nm. (d) ThT fluorescence of WT OLF compared to various reaction fractions considered in this study. (e) Reducing, denaturing SDS-PAGE analysis of fractions used in (d).

observed by negative stain TEM. Rather, cryo-EM imaging showed an abundance of small (4 nm) particles, more consistent with OLF monomer than a larger species (Figure 2b). However, this species was too small for high-resolution 3D single-particle reconstruction to determine the extent to which the species is native or partially folded (not shown).

Unexpectedly, there were sections of the cryo-EM grid that showed the presence of 2D-crystalline arrays in a halo in the middle of certain grid holes (Figure 2c). Single-particle analysis on these images allowed for the reconstruction of apparent trimers distinct from the crystalline array, seemingly forming at the barrier between the arrays and the monomeric bulk (Figure 2d and Table 1). These trimers are notably different from the donut-like species observed by negative stain TEM. It is possible that monomeric OLF adopts different nucleation states dependent on the specific chemical environments and that the apparent trimers are fragments of the 2D-crystalline arrays not observed by

negative stain TEM due to the unique conditions introduced during blot-free vitrification. To our knowledge this is the first report of such a phenomenon. In all, electron microscopy imaging agrees with the previous analysis (Figure 1e) that the bulk supernatant after fibrillization is composed of monomeric OLF, but additionally shows that monomers can form different oligomeric polymorphs under differing chemical environments.

### 2.3 | Additional characterization of soluble OLF species after fibrillization reveals some higher-ordered species and confirms preponderance of native OLF

Since the resolution of single-particle cryo-EM reconstruction is insufficient to assess the detailed molecular structure of the remaining soluble species we turned to other biophysical techniques. First, we used



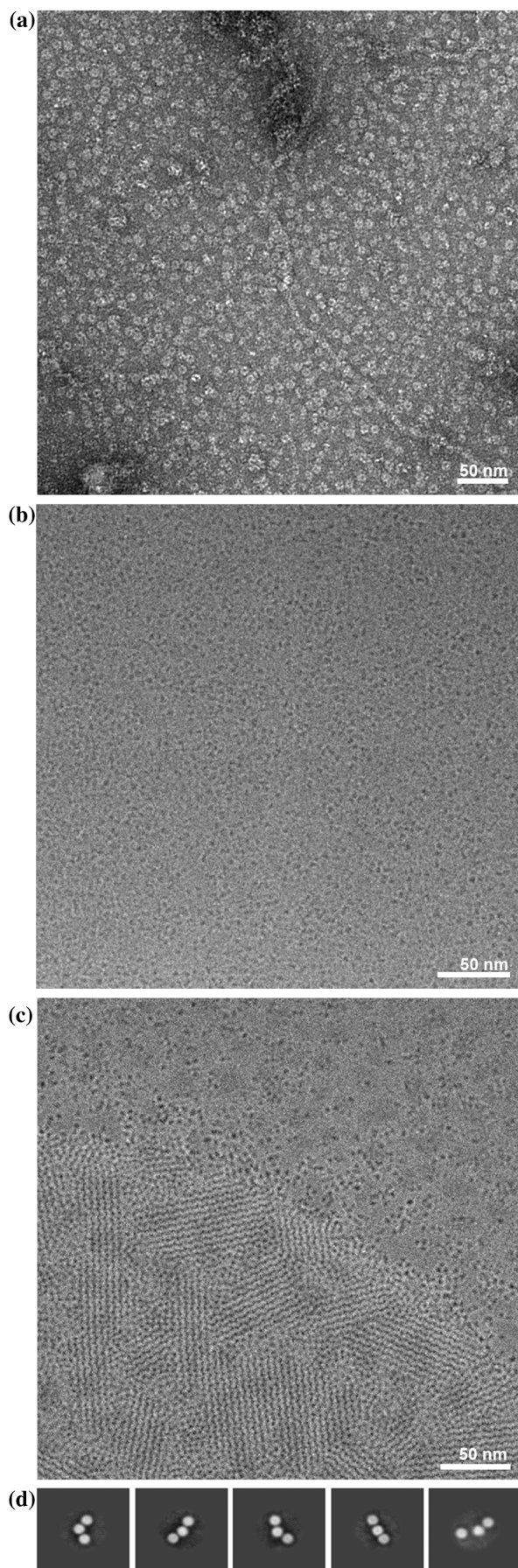


**TABLE 1** Cryo-EM data collection and reconstruction parameters.

Microscope	Titan Krios (Thermo Fisher Scientific)
Camera	DE Apollo 3
Acceleration voltage (kV)	300
Magnification	$\times 47,000$
Defocus range ( $\mu\text{m}$ )	$-1.5$ to $-3.5$
Number of movies	944
Number of frames/movie	120
Total electron dose ( $\text{e}^-/\text{\AA}$ )	60
Pixel size ( $\text{\AA}$ )	0.97

sedimentation velocity analytical ultracentrifugation (AUC) to fractionate the species present in our mixture. In line with denaturing SDS-PAGE analysis (Figure 1e), sedimentation velocity monitoring absorption at 280 nm shows that the end-point fibril mixture is composed of one major species at 2.58 S, corresponding to  $\sim 30$  kDa monomeric OLF (Figure 3a and Table 2). Consistent with the observation that oligomers of other amyloidogenic proteins range in size (Pieri et al. 2016), minor additional species were observed. These species are well described by an elongated trimer (5.3 S) and an elongated pentamer (7.4 S) (Figure 3a and Table 2). While a linear array of monomers is consistent with the experimental sedimentation coefficients and the 2D class averages from the 2D arrays (Figure 2d), suggesting that the intermediate species may be prefibrillar or pre-crystalline, other arrangements that account for partially folded state(s) are also possible.

Second, intrinsic tryptophan fluorescence of the OLF fibril sample ( $\lambda_{\text{max}}$  341–342 nm) is only slightly shifted from that of WT OLF ( $\lambda_{\text{max}}$  339 nm; Figure 3b). This result suggests that the primary species observed in AUC is WT-like. We note that both techniques require significant dilution of the sample, which could cause the dissociation of any transient oligomers.

Third, we tested whether the bulk of the OLF remaining in solution retained the native OLF structure. We filtered the OLF fibril supernatant sample and conducted crystallization trials. Crystals grew in conditions known for WT OLF (Saccuzzo et al. 2024b). The newly

**FIGURE 2** Visualization of OLF fibril mixture by TEM and cryo-EM. (a) Representative negative stain TEM image of the end-point fibril mixture. Fibrils are found on the grid surrounded by  $\sim 10$  nm species with an apparent central pore. Scale bar is 50 nm. (b) Representative cryo-EM grid of fibril mixture. Particles are  $\sim 4$  nm in diameter. Scale bar 50 nm. (c) Representative cryo-EM grid of fibril mixture forming 2D-crystalline arrays. Scale bar 50 nm. (d) 2D class averages of apparent trimers forming at the edge of the crystalline arrays.



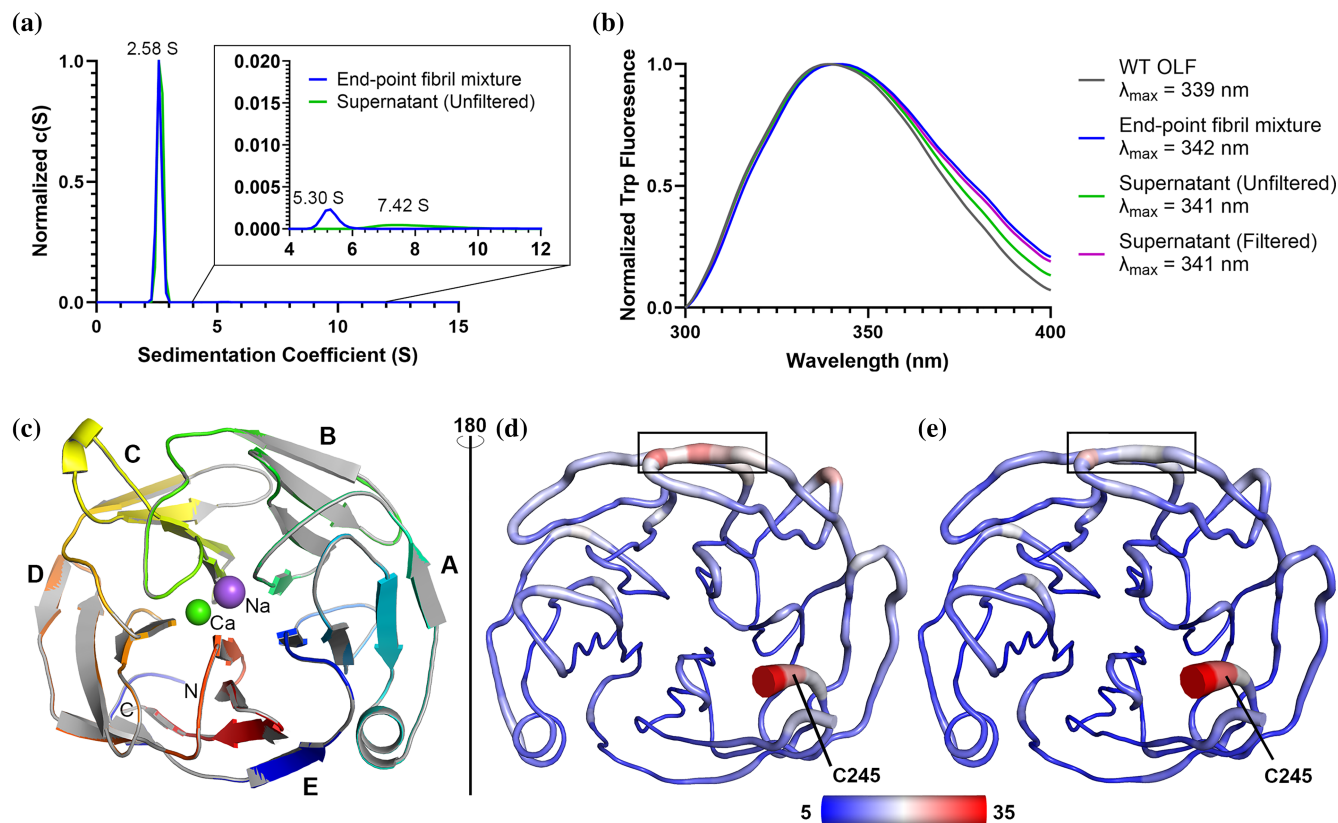


**FIGURE 3** Characterization of heterogeneous OLF supernatant. (a) Sedimentation velocity analytical ultracentrifugation of end-point fibril mixture (blue) and unfiltered supernatant (green). The predominant species in both samples has a sedimentation coefficient of 2.58 S. The inset shows a zoomed graph to capture the lowly prevalent species in both samples: 5.3 S for the end-point mixture and 7.4 S for the supernatant. (b) Intrinsic tryptophan fluorescence emission spectra and  $\lambda_{\text{max}}$  values for native WT OLF, end-point fibril mixture, unfiltered and filtered supernatant. (c) Overlay of 1.45 Å crystal structure solved from filtered supernatant (PDB ID: 9DOZ, rainbow) with 1.27 Å WT OLF crystal structure (PDB ID: 8FRR, gray). The five propeller blades A–E are labeled radially. (d, e) B-factors mapped onto (d) 8FRR and (e) 9DOZ. B-factor range from low to high values (5–35) is colored blue to white to red.

**TABLE 2** Sedimentation velocity coefficient analysis.

Species	Calculated sedimentation coefficient (S)	Experimental sedimentation coefficient (S)	Calculated MW (kDa)	Experimental MW (kDa)
Monomer	2.9	2.6	30.1	26.7
Dimer	4.4	5.3	60.2	72.8
Trimer (linear)	5.48	5.3	90.2	87.2
Trimer (stacked)	5.69	5.3	90.1	84.0
Tetramer (linear)	6.32	7.4	120.1	140.6
Tetramer (stacked)	6.72	7.4	120.2	132.3
Pentamer (linear)	7.15	7.4	150.4	155.7
Pentamer (stacked)	7.75	7.4	150.3	143.3

solved 1.45 Å resolution crystal structure (PDB code 9DOZ) is isomorphous with and indistinguishable from WT OLF (PDB code 8FRR), with a root mean squared deviation of 0.06 Å (Figure 3c and Table 3). Cys245, which forms a disulfide bond with Cys433, has a somewhat higher thermal B-factor in the current structure

(WT, 8FRR = 25 Å<sup>2</sup>, Figure 3d and 9DOZ = 28 Å<sup>2</sup>, Figure 3e). However, this does not seem to be a significant difference because residues N410–L413, comprising a loop in blade C, have higher B-factors in our previous WT OLF structure compared to the current one. In summary, after incubation at 37°C with rocking

**TABLE 3** X-ray data collection and refinement statistics.

	PDB code 9DOZ
Resolution range	37.3–1.45 (1.51–1.45)
Space group	P 1 21 1
Unit cell	49.3 50.9 50.5 90 96.7 90
Total reflections	246311 (18272)
Unique reflections	42816 (3909)
Multiplicity	5.8 (4.7)
Completeness (%)	97.7 (89.5)
Mean I/sigma(I)	13.5 (2.83)
Wilson B-factor	10.7
R-merge	0.15 (0.72)
R-meas	0.16 (0.81)
R-pim	0.066 (0.36)
CC <sub>1/2</sub>	0.99 (0.72)
CC*	1 (0.91)
Reflections used in refinement	42759 (3902)
Reflections used for R-free	2006 (181)
R-work	0.17 (0.21)
R-free	0.20 (0.24)
CC (work)	0.97 (0.91)
CC (free)	0.95 (0.86)
Number of non-hydrogen atoms	2291
Macromolecules	2096
Ligands	2
Solvent	193
Protein residues	259
RMS (bonds)	0.005
RMS (angles)	0.87
Ramachandran favored (%)	96.9
Ramachandran allowed (%)	3.11
Ramachandran outliers (%)	0.00
Rotamer outliers (%)	0.43
Clashscore	1.20
Average B-factor	13.7
Macromolecules	12.9
Ligands	7.14
Solvent	22.7

for 66 h, what remains in the bulk solution after filtration is homogeneous enough to crystallize and retains native structure.

## 2.4 | <sup>1</sup>H-<sup>15</sup>N TROSY-HSQC spectrum of <sup>15</sup>N-labeled OLF fibril sample reveals a low population of non-native OLF in solution

To detect any low population misfolded state(s) missed by the previous biophysical characterization methods, we prepared the same fibril sample, but with <sup>15</sup>N-

labeled OLF to allow for characterization by solution NMR. NMR is a technique well suited to detect low abundance changes in chemical environment even in heterogeneous mixtures. The <sup>1</sup>H-<sup>15</sup>N TROSY-HSQC spectrum of the fibril reaction supernatant largely agrees with our previously published WT OLF spectrum (Saccuzzo et al. 2024b). However, differences are detected near the center of the proton dimension (~8 ppm), where the incubated sample spectrum is less resolved, indicating some degree of unfolding or non-native OLF structure that is distinct from the WT OLF sample (Figure 4a). The broadening and lack of resolution in the proton dimension of the supernatant OLF NMR spectrum are consistent with a decrease in foldedness or an increase in slower timescale dynamics. Figure 4b shows several spectral changes including the appearance of some new peaks. Only partial backbone resonance assignments (~60%) are available for WT OLF (Saccuzzo et al. 2024b); nevertheless, there are some identifiable residues that show significant spectral differences. For example, G268, which is located in the center of blade A in the OLF β-propeller structure, has increased intensity in the fibril supernatant spectrum (Figure 4c,d). Enhanced intensity is generally associated with either an increase in rigidity or increased flexibility and dynamics that result in faster exchange between conformational states. One interpretation of G268 is that the increased local transient fluctuations of non-stable higher-order oligomeric intermediates are detected in this region. Another interpretation of G268 spectral features is that, based on previous studies that identify that OLF undergoes an inside-out unfolding on the pathway to aggregation (Saccuzzo et al. 2024b), the fibril reaction supernatant OLF sample experiences increased frequency of transient unfolding events near the core. We note that both interpretations would represent distinct signatures along the aggregation pathway. In contrast to G268, some resonances, like I499, are relatively unperturbed. This finding is notable because of links to severe pathogenicity upon mutation (I499F) (Adam et al. 1997). Since solution NMR does not generally report on insoluble species, the observed deviations that arise from natively folded OLF are due to soluble species.

## 3 | DISCUSSION

The molecular nature of pre-fibrillar intermediates on the way to the maturation of insoluble amyloid fibrils has been the subject of intense research inquiry (Chiti and Dobson 2017). However, characterization of such species is hampered by a high degree of heterogeneity and typically a short lifetime (Chiti and Dobson 2017). In this study, we sought to comprehend the extent of heterogeneity of species associated with de novo OLF fibrillization, a recent addition to the list of

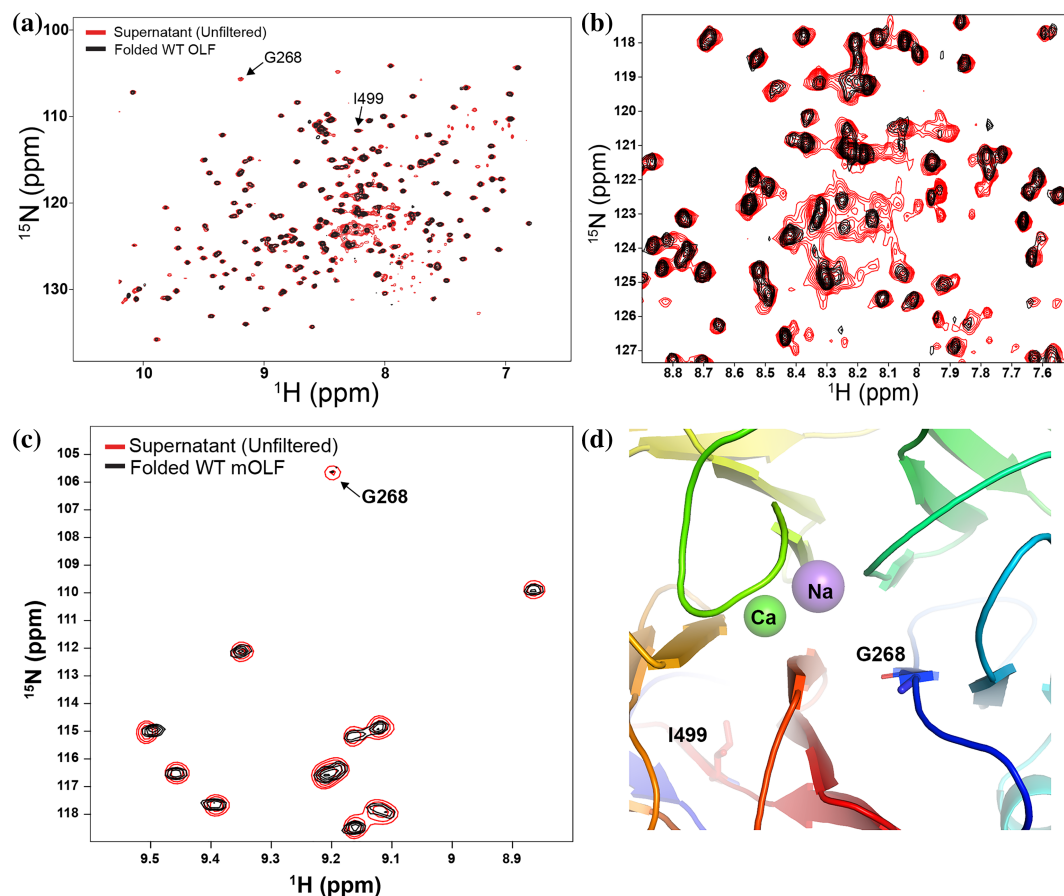


**FIGURE 4** Solution NMR shows deviations from WT structure. (a)  $^1\text{H}$ - $^{15}\text{N}$  TROSY-HSQC spectrum of unfiltered supernatant (red) compared to native WT OLF (black). Less resolved peaks near  $\sim 8$  ppm are indicative of partially unfolded protein in solution. (b) Zoom into center of proton dimension showing lack of resolved peaks. (c) A variety of spectral changes are present in the fibril supernatant spectrum, including increased intensity for G268 presumably indicative of faster time scale dynamics relative to WT OLF. (d) G268 highlighted on the OLF structure.

disease-associated proteins with a propensity toward misfolding. OLF is also an apt system to test themes and variations established with better studied amyloid-forming proteins.

We recently reported that the conversion of WT and mutant OLF into *de novo* fibrils competes with unfolding (Saccuzzo et al. 2024b) and our current study reveals new aspects of the fibrillization process. First, the ThT-positive species that we track over the course of the experiment is the mature fibril; the excess OLF remaining in solution after pelleting the fibrils does not yield a significantly higher ThT signal than the starting material. Second, the supernatant at the conclusion of the experiment is a heterogeneous mixture of species. A large fraction of the sample is natively folded OLF as evidenced by our ability to solve a crystal structure from a filtered solution, as well as native-like intrinsic fluorescence properties and predominance of a monomeric 30 kDa species seen in AUC from unfiltered samples. Although our TEM images showed a donut-shaped species reminiscent of oligomers of amyloid-forming proteins like amyloid- $\beta$ ,  $\alpha$ -synuclein, amylin, and serum amyloid A (Lashuel et al. 2002; Quist et al. 2005), and

a species seen for OLF in our initial characterization (Orwig et al. 2012), this appears to be unique to negative stain TEM grid preparation since it was not observed in cryo-EM. Instead, cryo-EM shows a preponderance of monomer in solution, but unexpectedly, also shows the presence of 2D-crystalline arrays. Perhaps the difference between the negative stain donut-shaped species and the cryo-EM crystalline arrays are results of the different chemical environments induced by heavy metal staining (Kiselev et al. 1990) versus blot-free vitrification.

Third, non-native OLF species were detected in solution. Possible OLF trimers and pentamers were seen by AUC, OLF trimers were seen in association with 2D crystalline arrays in cryo-EM, and a non-native fingerprint was seen in NMR. The hydrophobic collapse seen for the clarified supernatant is reminiscent of the collapse seen for disease-causing mutants, albeit not to the same extent. Notably, we have only ever observed low levels of OLF dimers in crosslinking experiments (Huard et al. 2019) so these higher ordered species are likely non-native. When considering the three possible roles of oligomers in fibril



formation—nucleated polymerization, nucleated conformational conversion, and off-pathway oligomers (Muschol and Hoyer 2023)—the observed halt of fibril nucleation would suggest that at least one of the polymorphic OLF species is/are off pathway, blocking fibril nucleation. This could explain the high concentrations of monomeric OLF remaining after removing the mature fibrils from the solution. The concept of a critical oligomer concentration suggests that after a certain concentration of monomer, fibril growth should change in favor of oligomer formation (Miti et al. 2015). If the oligomers formed at this stage are off-pathway, fibril nucleation would slow as would monomer consumption. Presumably, any on-pathway OLF oligomers are ephemeral as they are converted to fibrils and do not accumulate to levels that can be detected.

At 30 kDa, OLF is larger than most folded amyloid-forming proteins and for this reason there are likely more oligomeric polymorphs, both on- and off-pathway, compared to smaller proteins that form amyloid. One might also anticipate more fibril structures are possible under different conditions. Our studies of OLF fibrillization to date have been limited to the relatively mild conditions reported herein due to their highly favorable and reproducible kinetic profile for biophysical characterization. Future work will focus on finding conditions that allow for the accumulation and detection of a dominant on-pathway polymorph and strengthening the connection to mutant myocilin misfolding in cells. In the long term, a detailed understanding of the myocilin species responsible for cytotoxicity could lead to new therapeutic avenues for myocilin-associated glaucoma.

## 4 | METHODS

### 4.1 | Protein purification

OLF was recombinantly expressed and purified as described previously (Donegan et al. 2015) with minor modifications. Briefly, Rosetta-gami 2(DE3) cells (Novagen) transformed with plasmids were grown in Superior broth (US Biological) supplemented with 60 µg/mL of ampicillin and 34 µg/mL of chloramphenicol. Cultures were induced at an OD<sub>600</sub> of 1.5 at 18°C with 0.5 mM isopropyl-β-D-thiogalactopyranoside and 100 mM CaCl<sub>2</sub>, and cells were allowed to grow for 16 h. The cells were pelleted, flash frozen in liquid nitrogen, and stored at −80°C. Protein was purified by amylose affinity chromatography and size-exclusion chromatography as reported previously (Donegan et al. 2012). Purified OLF was stored in PGF buffer (10 mM Na<sub>2</sub>HPO<sub>4</sub>/KH<sub>2</sub>PO<sub>4</sub>, 0.2 M NaCl, pH 6.8). Purity was assessed by standard 12% SDS-PAGE analysis using stain-free gels visualized with the Bio-Rad ChemiDoc MP imaging System.

<sup>15</sup>N labeled OLF for NMR was expressed as described previously (Saccuzzo et al. 2024b) and purified in the same way as unlabeled OLF.

### 4.2 | Oligomer preparation

Schematic of oligomer preparation shown in Figure 1a. Oligomer reactions were prepared by adding 200 µL of 200 µM purified OLF in PGF buffer to a 0.65 mL microcentrifuge tube (VWR). This tube was sealed with parafilm and rocked on a 3D rocker at 37°C for 66 h. After 66 h, the sample turned cloudy with an insoluble species that readily settled out of solution. The end-point fibril mixture was stored at 4°C. The supernatant was separated after brief benchtop centrifugation at 2000g. Where indicated, the supernatant was filtered through a 0.22 µm PVDF syringe filter (Millex) to remove large aggregates. The insoluble end-point fibrils were washed after removing the supernatant by adding 30 µL of PGF buffer, resuspending the fibrils, and then brief benchtop centrifugation. This process was repeated 7 times, until the wash supernatant had an A<sub>280</sub> < 0.1.

ThT fluorescence was followed using a Horiba FluoroMax spectrofluorometer equipped with a peltier temperature control system. For the growth curve, 1 µM ThT was added to a 4.75 µL aliquot of the end-point reaction mixture diluted in 45 µL of water at each time-point. Endpoint fluorescence was measured with an excitation wavelength of 440 nm ± 1 nm and an emission wavelength of 485 nm ± 1 nm. ThT fluorescence before and after centrifugation was measured by adding 10 µM ThT to 47.5 µL of protein diluted 1:1 with buffer using the same excitation and emission parameters as for the growth curve. Values were scaled according to sample concentration as determined by a Bradford Assay (Bradford 1976) and then normalized to the fluorescence intensity of the end-point fibril mixture. Raw fluorescence data has been uploaded to Figshare (DOI: [10.6084/m9.figshare.28183835](https://doi.org/10.6084/m9.figshare.28183835)).

### 4.3 | Negative stain TEM

Negative stain TEM grids were prepared with washed fibrils (Figure 1b) resuspended in 4 µL of fresh PGF buffer. Two microliter of washed fibrils were placed on a 400 mesh Quantifoil carbon-coated copper grid. Grids were incubated for 1 min at room temperature. Excess sample was blotted away with Whatman filter paper. Grids were washed with 10 µL water for 1 min and stained with 10 µL of 1% uranyl acetate for 1 min. Dried grids were imaged on a 120 kV JEOL JEM-1400 TEM with a Gatan OneView camera.

Negative stain grids of the end-point fibril mixture (Figure 2a) were prepared with non-diluted sample

before any separation steps. Three microliters of sample was placed on a 400 mesh Quantifoil carbon-coated copper grid that was glow discharged for 30 s at 15 mA on a PELCO easiGlow instrument (TED PELLA). The grids were incubated for 1 min at room temperature. Excess sample was blotted away with Whatman filter paper. Grids were washed with 10  $\mu$ L water for 1 min and stained with 10  $\mu$ L 0.75% uranyl formate for 1 min. Dried grids were imaged on a FEI Talos 120 kV TEM with LaB6 and 4 k Ceta detector at the Emory University Robert P. Apkarian Integrated Electron Microscopy core.

#### 4.4 | Cryogenic-electron microscopy

End-point fibril mixture samples were sent to the Southeastern Center for Microscopy of Macromolecular Machines (SECM4) for cryo-EM grid preparation and data collection. Blot-free sample vitrification was performed using a Chameleon and Quantifoil Active self-wicking grids (SPT labtech). Grids were prepared with 1:5 (v:v) end-point fibril mixture diluted with PGF buffer. The grid was glow discharged at 25 mA for 75 s with a 702 ms plunge time. Data was collected on a FEI Titan Krios 300 kV TEM equipped with a direct electron DE Apollo 3 camera (see Table 2).

Super resolution data were processed using CryoSPARC (Punjani et al. 2017). In brief, the motion and CTF of acquired micrographs were corrected using the Patch Motion correction and Patch CTF correction jobs, respectively. Micrographs were subsequently filtered by CTF parameters, using 8 Å resolution as a cutoff to ensure that only the highest quality micrographs were processed further. The initial particle picking was performed using Topaz (Bepler et al. 2019; Bepler et al. 2020), a neural network picker with a pre-trained model to pick particles in a ~10% subset of micrographs. The particles were extracted and subjected to several rounds of 2D classification to remove suboptimal particles and retain the particles representing the apparent OLF trimers. These selected particles were used to train a new Topaz model, which was subsequently optimized and used to pick particles from the entire dataset. The particles in thick ice were removed through several rounds of 2D classification.

#### 4.5 | Analytical ultracentrifugation

Sedimentation velocity measurements were performed using a Beckman Optima AUC equipped with an An-50

Ti analytical rotor. The unfiltered supernatant and the end-point fibril mixture were each diluted to an  $A_{280} = \sim 0.5$ . The wavelength used for sample detection was 280 nm and the instrument was run at 42,000 rpm at 25°C for 12 h. Data were processed using the program SEDFIT (Schuck 2004) and key buffer properties were calculated with SEDNTERP (Philo 2023). The partial specific volume of OLF monomer and theoretical sedimentation coefficients for OLF monomer and multimers were calculated with HULLRAD (Fleming and Fleming 2018) using the WT OLF crystal structure PDB ID: 4WXQ as an input model. Data fitting parameters are listed in Table 4.

#### 4.6 | Fluorescence spectroscopy

The folded state of the protein in the supernatant was assessed using intrinsic tryptophan fluorescence as reported previously (Saccuzzo et al. 2024b) with minor modifications. Four independent oligomer reactions were prepared. Measurements were recorded for WT OLF ( $n = 5$ ), end-point reaction mixture ( $n = 2$ ), unfiltered supernatant ( $n = 8$ ), and filtered supernatant ( $n = 3$ ).

Fluorescence spectra were measured at 25°C on a Horiba FluoroMax spectrofluorometer equipped with a Peltier temperature control system. Emission spectra were measured from 300 to 400 nm  $\pm$  1 nm at 1 nm intervals with an excitation wavelength of 295  $\pm$  1 nm. Each recorded wavelength emission maximum ( $\lambda_{\max}$ ) value is the average of five scans on the same sample. Spectra were first smoothed according to a second-order polynomial averaging five neighbors. The emission wavelength corresponding to the highest fluorescence intensity was recorded as  $\lambda_{\max}$ . Fluorescence was normalized to the max of each individual sample for graphing purposes. Data smoothing and analysis was performed in GraphPad Prism v9.

#### 4.7 | X-ray crystallography

The supernatant was filtered with a 0.22  $\mu$ m syringe filter. The filtered protein was buffer exchanged into 10 mM HEPES, 0.2M NaCl pH 7.2 and concentrated to 10 mg/mL with a 10-kDa MWCO centrifugal filter. The reservoir solution of 500  $\mu$ L was composed of 10% PEG 8000 and 0.1M MgCl<sub>2</sub>. Hanging drops of 4  $\mu$ L were prepared on plastic cover slips at a 1:1 (v:v) ratio of protein and the reservoir solution. Crystals were observed after 4 days of incubation at 16°C. Crystals were harvested and cryoprotected in the reservoir

**TABLE 4** Sedimentation velocity data fitting parameters.

	Buffer density (g/mL)	Buffer viscosity (Poise)	Vbar (mL/g)	Frictional ratio
WT OLF (PDB ID: 4WXQ)	1.00896	0.01026	0.735	1.21102

solution supplemented with 20% glycerol followed by flash-cooling in liquid nitrogen.

Data were collected on the NYX beamline 19-D at Brookhaven National Laboratory National Synchrotron Light Source II (NSLS-II) and were processed using HKL-2000 (Otwinowski and Minor 1997). Molecular replacement was performed with *Phaser* (McCoy 2007) using the polypeptide chain of WT OLF (PDB ID: 4WXQ) as a search model. The model was built and refined using *Coot* (Emsley et al. 2010) and *phenix.refine* (Afonine et al. 2012). Figures were prepared in PyMOL. The structure was deposited in the PDB with accession code 9DOZ. Data collection statistics are reported in Table 3.

## 4.8 | NMR

$^1\text{H}$ - $^{15}\text{N}$  TROSY-HSQC spectra were collected on a Bruker Avance III HD 800 MHz  $^1\text{H}$  spectrometer equipped with a TCI helium temperature cryoprobe. NMR data were collected with Topspin 3.5 pl5at 25°C using a 3-mm NMR tube with 10%  $\text{D}_2\text{O}$ . The  $^{15}\text{N}$  labeled unfiltered supernatant sample was 195  $\mu\text{L}$  of 150  $\mu\text{M}$  in PGF buffer. Data were processed in NMRPipe (Delaglio et al. 1995). The soluble HSQC spectrum was collected under the same conditions as previously published (Saccuzzo et al. 2024b). Comparison between the supernatant of the fibrillization reaction and the soluble WT OLF spectra were analyzed with CCPNMR Analysis (Skinner et al. 2016).

## AUTHOR CONTRIBUTIONS

**Hailee F. Scelsi:** Conceptualization; investigation; visualization; validation; formal analysis; data curation; writing – original draft. **Emily G. S. Close:** Conceptualization; data curation; formal analysis; visualization; investigation; validation. **Dustin J. E. Huard:** Investigation; validation; visualization; writing – review and editing. **Elijah Dunn:** Investigation; writing – review and editing. **Nebojša Bogdanović:** Writing – review and editing. **Sonali H. W. Mudiyansele:** Investigation; writing – review and editing. **Arshay Grant:** Investigation; writing – review and editing. **Scott M. Stagg:** Funding acquisition; investigation; writing – review and editing; formal analysis; supervision; project administration. **Ingeborg Schmidt-Krey:** Investigation; funding acquisition; writing – review and editing; formal analysis; supervision. **Wade D. Van Horn:** Investigation; funding acquisition; writing – original draft; formal analysis; supervision; project administration. **Raquel L. Lieberman:** Investigation; conceptualization; funding acquisition; writing – original draft; supervision; visualization; project administration.

## ACKNOWLEDGMENTS

This work was funded by NIH grant R01EY021205 to R.L.L. and R35GM141933 to W.V.H. Access to NYX

beamline 19-D at the National Synchrotron Light Source II (NSLS-II) was provided through the Southeast Regional Collaborative Access Team (SER-CAT). SER-CAT is supported by its member institutions, equipment grants (S10\_RR25528, S10\_RR028976, and S10\_OD027000) from the National Institutes of Health, and funding from the Georgia Research Alliance. NSLS-II is a U.S. Department of Energy (DOE) Office of Science User Facility operated for the DOE office of Science by Brookhaven National Laboratory under contract No. DE-SC0012704. Use of the NYX beamline 19-ID at the was supported by the New York Structural Biology Center. NYX detector instrumentation was supported by grant S10OD030394 through the office of the Director, National Institutes of Health. The Southeastern Center for Microscopy of Macromolecular Machines (SECM4) is funded by NIH R24GM145964. Negative stain TEM imaging in this study was supported by Emory University Robert P. Apkarian Integrated Electron Microscopy Core Facility (RRID: SCR\_023537), which is subsidized by the School of Medicine and Emory College of Arts and Sciences. Additional support was provided by the Georgia Clinical & Translational Science Alliance of the National Institutes of Health under award number UL1TR000454. The content is solely the responsibility of the authors and does not necessarily represent the official views of the National Institutes of Health.

## DATA AVAILABILITY STATEMENT

The data that support the findings of this study are openly available in Figshare at <https://figshare.com/s/c8702a6b65b92073a1a3>.

## ORCID

Wade D. Van Horn  <https://orcid.org/0000-0002-2493-5578>

Raquel L. Lieberman  <https://orcid.org/0000-0001-9345-3735>

## REFERENCES

- Adam MF, Belmouden A, Binisti P, Brézin AP, Valtot F, Béchetoille A, et al. Recurrent mutations in a single exon encoding the evolutionarily conserved olfactomedin-homology domain of TIGR in familial open-angle glaucoma. *Hum Mol Genet.* 1997;6(12):2091–7.
- Afonine PV, Grosse-Kunstleve RW, Echols N, Headd JJ, Moriarty NW, Mustyakimov M, et al. Towards automated crystallographic structure refinement with phenix.refine. *Acta Crystallogr D Biol Crystallogr.* 2012;68:352–67.
- Bepler T, Kelley K, Noble AJ, Berger B. Topaz-Denoise: general deep denoising models for cryoEM and cryoET. 2020. *bioRxiv* 838920.
- Bepler T, Morin A, Rapp M, Brasch J, Shapiro L, Noble AJ, et al. Positive-unlabeled convolutional neural networks for particle picking in cryo-electron micrographs. *Nat Methods.* 2019;16(11):1153–60.
- Bradford MM. A rapid and sensitive method for the quantitation of microgram quantities of protein utilizing the principle of protein-dye binding. *Anal Biochem.* 1976;72:248–54.
- Chiti F, Dobson CM. Protein misfolding, amyloid formation, and human disease: a summary of progress over the last decade. *Annu Rev Biochem.* 2017;86:27–68.



- Delaglio F, Grzesiek S, Vuister GW, Zhu G, Pfeifer J, Bax A. NMRPipe: a multidimensional spectral processing system based on UNIX pipes. *J Biomol NMR*. 1995;6(3):277–93.
- Donegan RK, Hill SE, Freeman DM, Nguyen E, Orwig SD, Turnage KC, et al. Structural basis for misfolding in myocilin-associated glaucoma. *Hum Mol Genet*. 2015;24(8):2111–24.
- Donegan RK, Hill SE, Turnage KC, Orwig SD, Lieberman RL. The glaucoma-associated olfactomedin domain of myocilin is a novel calcium binding protein. *J Biol Chem*. 2012;287(52):43370–7.
- Emsley P, Lohkamp B, Scott WG, Cowtan K. Features and development of Coot. *Acta Crystallogr D Biol Crystallogr*. 2010;66:486–501.
- Fändrich M. Oligomeric intermediates in amyloid formation: structure determination and mechanisms of toxicity. *J Mol Biol*. 2012;421(4):427–40.
- Fleming PJ, Fleming KG. HullRad: fast calculations of folded and disordered protein and nucleic acid hydrodynamic properties. *Biophys J*. 2018;114(4):856–69.
- Hill SE, Donegan RK, Lieberman RL. The glaucoma-associated olfactomedin domain of myocilin forms polymorphic fibrils that are constrained by partial unfolding and peptide sequence. *J Mol Biol*. 2014;426(4):921–35.
- Huard DJE, Jonke AP, Torres MP, Lieberman RL. Different Grp94 components interact transiently with the myocilin olfactomedin domain in vitro to enhance or retard its amyloid aggregation. *Sci Rep*. 2019;9(1):12769.
- Joe MK, Sohn S, Hur W, Moon Y, Choi YR, Kee C. Accumulation of mutant myocilins in ER leads to ER stress and potential cytotoxicity in human trabecular meshwork cells. *Biochem Biophys Res Commun*. 2003;312(3):592–600.
- Kayed R, Head E, Thompson JL, McIntire TM, Milton SC, Cotman CW, et al. Common structure of soluble amyloid oligomers implies common mechanism of pathogenesis. *Science*. 2003;300(5618):486–9.
- Kiselev NA, Sherman MB, Tsuprun VL. Negative staining of proteins. *Electron Microsc Rev*. 1990;3(1):43–72.
- Lashuel HA, Hartley D, Petre BM, Walz T, Lansbury PT. Amyloid pores from pathogenic mutations. *Nature*. 2002;418(6895):291.
- McCoy AJ. Solving structures of protein complexes by molecular replacement with Phaser. *Acta Crystallogr D Biol Crystallogr*. 2007;63:32–41.
- Miti T, Mulaj M, Schmit JD, Muschol M. Stable, metastable, and kinetically trapped amyloid aggregate phases. *Biomacromolecules*. 2015;16(1):326–35.
- Muschol M, Hoyer W. Amyloid oligomers as on-pathway precursors or off-pathway competitors of fibrils. *Front Mol Biosci*. 2023;10:1120416. <https://doi.org/10.3389/fmolb.2023.1120416>
- Orwig SD, Perry CW, Kim LY, Turnage KC, Zhang R, Vollrath D, et al. Amyloid fibril formation by the glaucoma-associated olfactomedin domain of myocilin. *J Mol Biol*. 2012;421(2–3):242–55.
- Otwinowski Z, Minor W. Processing of X-ray diffraction data collected in oscillation mode. *Methods in enzymology*. Volume 276. Cambridge: Academic Press; 1997. p. 307–26.
- Philo JS. SEDNTERP: a calculation and database utility to aid interpretation of analytical ultracentrifugation and light scattering data. *Eur Biophys J*. 2023;52(4):233–66.
- Pieri L, Madiona K, Melki R. Structural and functional properties of prefibrillar  $\alpha$ -synuclein oligomers. *Sci Rep*. 2016;6(1):24526.
- Punjani A, Rubinstein JL, Fleet DJ, Brubaker MA. cryoSPARC: algorithms for rapid unsupervised cryo-EM structure determination. *Nat Methods*. 2017;14(3):290–6.
- Quist A, Doudevski I, Lin H, Azimova R, Ng D, Frangione B, et al. Amyloid ion channels: a common structural link for protein-misfolding disease. *Proc Natl Acad Sci U S A*. 2005;102(30):10427–32.
- Saccuzzo EG, Mebrat MD, Scelsi HF, Kim M, Ma MT, Su X, et al. Competition between inside-out unfolding and pathogenic aggregation in an amyloid-forming  $\beta$ -propeller. *Nat Commun*. 2024b;15(1):155.
- Saccuzzo EG, Robang AS, Gao Y, Chen B, Lieberman RL, Paravastu AK. Evidence for S<sub>331</sub>-G-S-L within the amyloid core of myocilin olfactomedin domain fibrils based on low-resolution 3D solid-state NMR spectra. 2024a. *bioRxiv* 2024.08.09.606901.
- Schuck P. A model for sedimentation in inhomogeneous media. I. Dynamic density gradients from sedimenting co-solutes. *Biophys Chem*. 2004;108(1–3):187–200.
- Skinner SP, Fogh RH, Boucher W, Ragan TJ, Mureddu LG, Vuister GW. CcpNmr AnalysisAssign: a flexible platform for integrated NMR analysis. *J Biomol NMR*. 2016;66(2):111–24.
- Stamer WD, Clark AF. The many faces of the trabecular meshwork cell. *Exp Eye Res*. 2017;158:112–23.
- Wiggs JL, Pasquale LR. Genetics of glaucoma. *Hum Mol Genet*. 2017;26(R1):R21–7.
- Yam GH-F, Gaplovska-Kysela K, Zuber C, Roth J. Aggregated myocilin induces russell bodies and causes apoptosis: implications for the pathogenesis of myocilin-caused primary open-angle glaucoma. *Am J Pathol*. 2007;170(1):100–9.

**How to cite this article:** Scelsi HF, Close EGS, Huard DJE, Dunn E, Bogdanović N, Mudiyansele SHW, et al. Detection of non-native species formed during fibrillization of the myocilin olfactomedin domain. *Protein Science*. 2025;34(4):e70063. <https://doi.org/10.1002/pro.70063>